

MODELING CREEP DEFORMATION AND PREDICTING RUPTURE LIFE OF STRESS-CONCENTRATED DZ411 SUPERALLOY COMPONENTS USING A THREE-STAGE CREEP FRAMEWORK

Zhikun Li[1], Dasheng Wei[1], Wu Zeng[2], KarKash Alynur[1], Xin Liu[1], Bin Zhao[1], Suqi Li[1], Li Ma[3] & Shun Yang[1,4,5,6,*]

[1]School of Energy and Power Engineering, Beihang University, Beijing, China
[2]Advanced Gas Turbine Laboratory, Institute of Engineering Thermophysics, Chinese Academy of Sciences, Beijing, China
[3]Shaanxi KUCH ENERGY Technology Co., Ltd., Xi'an, China
[4]State Key Laboratory for Strength and Vibration of Mechanical Structures, Xi'an Jiaotong University, Xi'an, China
[5]State Key Laboratory of Structural Analysis for Industrial Equipment, Dalian University of Technology, Dalian, China
[6]State Key Laboratory of High Performance Ceramics and Superfine Microstructure, Shanghai Institute of Ceramics, Chinese Academy of Science, Shanghai, China

Abstract

To address creep-induced deformation and failure in high-temperature components of gas turbine engines, this study investigated the creep rupture life of stress-concentrated structures subjected to complex stress states. A three-stage creep constitutive model was employed to simulate creep deformation in critical regions of notched geometries. Building upon this framework, a rupture life prediction methodology was developed that incorporates the stress triaxiality factor and creep-induced stress relaxation effects. The proposed approach was validated against high-temperature creep tests conducted on circumferentially notched round bar specimens made of the directionally solidified nickel-based superalloy DZ411. The results showed that the finite element analysis based on the three-stage creep model accurately captured the elastoplastic deformation behavior of circumferentially notched round bar specimens. In stress-concentrated zones, significant stress relaxation occurred during creep, leading the equivalent stress to gradually stabilize over time. Furthermore, the predicted rupture lives agreed well with experimental data, with all predictions falling within a scatter band of ±2.

Keywords: Creep; Notch softening; Finite element analysis; Rupture life; Directionally solidified superalloy

1. Introduction

Owing to their exceptional mechanical properties at elevated temperatures, nickel-based superalloys have been widely utilized in the manufacturing of advanced turbine blades [1, 2]. To meet stringent cooling requirements, turbine blades are designed with intricate structural configurations, which inevitably induce complex multiaxial stress states during service. In practical blade architectures, various geometric features such as pin-fins (pedestals), staggered ribs, trailing-edge discharge windows, and film cooling holes are extensively integrated. These irregular and highly non-uniform geometries precipitate severe localized stress concentrations. At a given temperature, regions under elevated stress exhibit accelerated creep strain accumulation, whereas low-stress regions experience much slower deformation. Consequently, the low-strain regions structurally constrain the deformation of adjacent high-strain zones, driving a continuous redistribution of local stresses [3].

Over prolonged service durations, this creep-driven mismatch triggers significant stress relaxation, manifested by a marked decline in peak stress levels and a reduction in stress gradients near the notch roots. In high-temperature structural components, such stress relaxation effects are highly beneficial, as they alleviate local stress concentrations, suppress the macroscopic creep strain rate, and ultimately extend the creep-rupture life of the material.

Harnessing these stress relaxation characteristics has therefore become a pivotal strategy in aerospace, energy, and advanced manufacturing sectors to optimize the structural performance and extend the service life of critical high-temperature components.

Under sustained high-temperature loading, the creep deformation of these alloys exhibits pronounced time-dependent characteristics, strictly progressing through three sequential stages governed by the competitive synergy of underlying microstructural mechanisms. In the primary (transient) stage, the macroscopic strain rate continuously decays as rapid dislocation multiplication and entanglement induce a dominant strain-hardening effect that outpaces thermal recovery.

Subsequently, the material enters the critical secondary (steady-state) stage, which is characterized by a nearly constant minimum creep rate sustained by a dynamic equilibrium between work hardening and diffusion-controlled recovery processes, such as dislocation climb and cross-slip. Finally, the tertiary stage exhibits a non-linear, exponential acceleration in strain rate culminating in catastrophic fracture; this rapid macro-mechanical degradation is fundamentally driven by a positive feedback loop between localized necking and irreversible microstructural damage, where vacancy condensation and grain boundary sliding trigger micro-void nucleation, coalescence, and subsequent intergranular cracking.

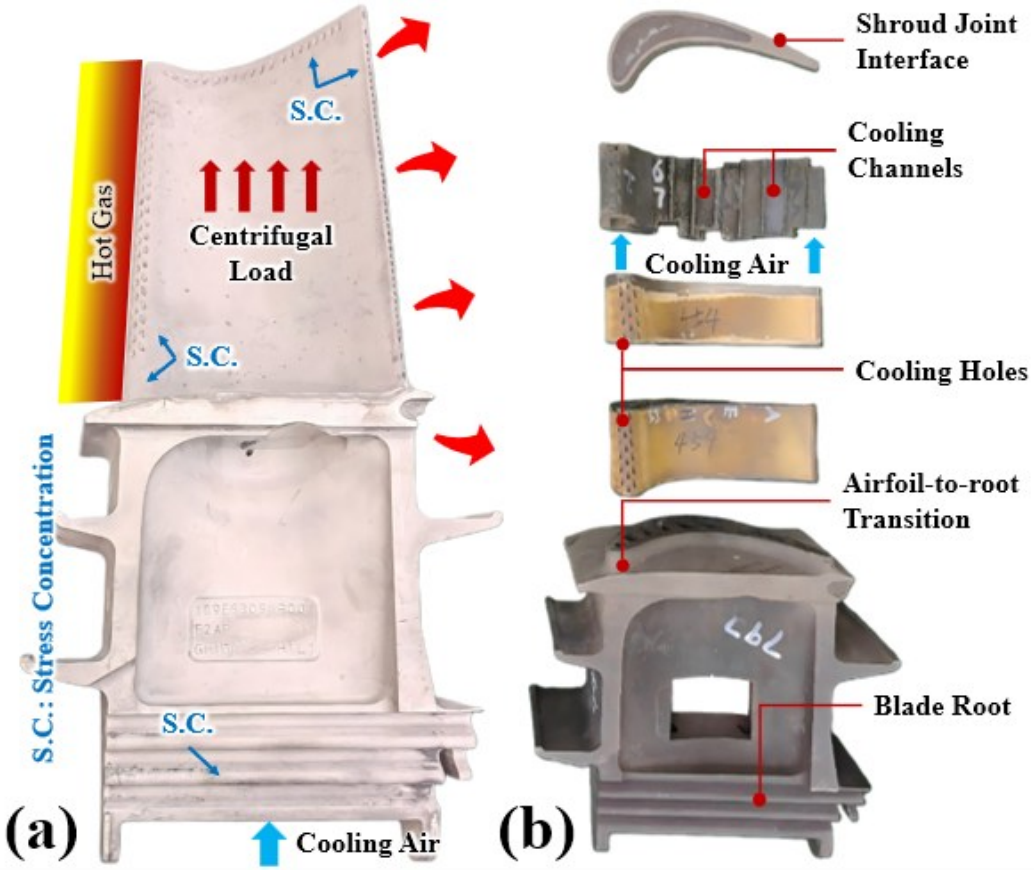


Figure 1 – Typical structure and loading conditions of a turbine blade: (a) service environment and stress concentration (S.C.) locations, and (b) key geometric features.

Despite these advancements, the majority of existing life prediction methodologies remain heavily reliant on standard uniaxial creep data, rendering them inherently incapable of capturing the transient, multiaxial stress states developed within actual engineering components. Creep behavior under complex, localized multiaxial loading exhibits fundamental mechanistic deviations from uniaxial conditions, which severely compromises the predictive fidelity of traditional approaches [4]. To bridge this critical knowledge gap, the present study introduces a robust FEA-based framework incorporating a comprehensive three-stage creep constitutive model. This methodology is explicitly formulated to track the spatial-temporal stress evolution and accurately predict the high-temperature rupture life of structural components featuring severe geometric stress concentrations.

2. Finite Element Analysis Based on a Three-Stage Creep Model

2.1 Creep Model

At present, accurately predicting the creep deformation and rupture life of complex components remains a formidable challenge. Extant creep deformation theories predominantly focus on characterizing the steady-state (secondary) stage or the transient-to-steady-state (primary and secondary) regimes. Creep constitutive models capable of coupling damage evolution to fully describe the complete three-stage characteristics of directionally solidified materials remain deficient, rendering them inadequate for precisely capturing the rapid acceleration of deformation during the tertiary stage.

Based on the framework of the θ-projection method, a creep constitutive model utilizing normalized parameters is proposed in this study, which is expressed as follows:

$$\varepsilon_c = \eta_1(1-e^{-\eta_4\zeta}) + \eta_2\zeta + \eta_3\zeta^{\eta_5} \tag{1}$$

Nevertheless, owing to an insufficient representation of damage evolution, this formulation remains incapable of accurately describing the tertiary creep stage, particularly the characteristic microstructural softening behavior.

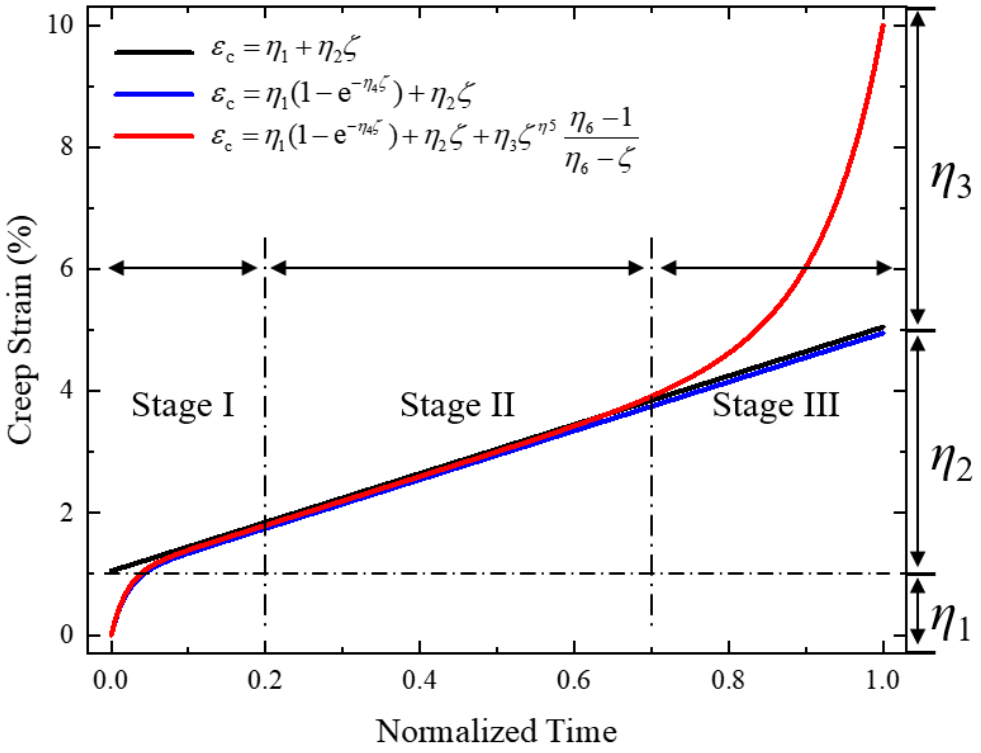


Figure 2 – Schematic description of the three-stage creep curve and model parameter definitions.

A normalized parameter creep model is introduced here to more reliably describe the full creep curve. The improved model effectively represents all three stages of creep deformation and provides robust fitting performance across a wide range of experimental data:

$$\varepsilon_c = \eta_1(1-e^{-\eta_4\zeta}) + \eta_2\zeta + \eta_3\zeta^{\eta_5}\frac{\eta_6-1}{\eta_6-\zeta} \tag{2}$$

Each term in Equation (2) corresponds to a distinct stage of creep deformation. Here, the normalized time is defined as

$$\zeta = t/t_c \left(\zeta \in [0,1]\right) \tag{3}$$

where t_c denotes the creep rupture lifetime under given temperature and stress conditions. The parameters η_i (i=1,2,3,4,5,6) are material-specific and depend on normalized stress $\sigma/\sigma_{0.2}$ and

normalized temperature T/T_m. The coefficients η_1, η_2, and η_3 represent the magnitude of the deformation in the primary, secondary, and tertiary stages, respectively. As ζ=1, the total creep rupture elongation satisfies:

$$\delta_c = \eta_1 + \eta_2 + \eta_3 \tag{4}$$

The parameter η_4 governs the shape of the primary creep stage, while η_5 and η_6 characterize the acceleration behavior during tertiary creep. The temperature and stress dependence of the six parameters η_i (i=1,2,3,4,5,6) is expressed as:

$$\ln \eta_i = a_i + b_i \frac{T}{T_m} + c_i \frac{\sigma}{\sigma_{0.2}} + d_i \frac{T}{T_m}\frac{\sigma}{\sigma_{0.2}} \tag{5}$$

Here, $\sigma/\sigma_{0.2}$ represents the stress normalized by the yield strength (with σ in MPa), and T/T_m is the temperature normalized by the material's melting point (with T in Kelvin).

2.2 Parameters Fitting

Depending on the material type, creep rupture lifetime can be predicted using either the Larson-Miller (L-M) model [5] or the Manson-Succop (M-S) [6]:

$$\lg t_c = g_1 + g_2 \frac{1}{T_R} + g_3 \frac{x}{T_R} + g_4 \frac{x^2}{T_R} + g_5 \frac{x^3}{T_R} \tag{6}$$

$$\lg t_c = g_1 + g_2 T_R + g_3 x + g_4 x^2 + g_5 x^3 \tag{7}$$

In both expressions, the reference temperature T_R is defined as:

$$T_R = (9/5\theta + 32) + 460 \tag{8}$$

where θ is the temperature in ℃, and x=lg σ, with σ expressed in MPa. Based on the initial creep test data, the L-M equation was used to fit the creep life parameters.

The corresponding parameters are summarized in Table 1 and implemented into finite element creep simulations.

Table 1 - Creep parameters (g1-g5) for the Larson-Miller model fitted under different conditions.

g_1	g_2	g_3	g_4	g_5
-20.46	217734.16	-191195.84	79498.19	-12079.44

The parameter identification procedure, illustrated in Figure 2, consists of the following steps:

First, the parameter η_2 is determined from the slope of the secondary creep stage, while η_1 is estimated based on the vertical position of the secondary creep curve, and η_3 is derived from the total rupture elongation as:

$$\eta_3 = \delta_c - \eta_1 - \eta_2 \tag{9}$$

The black line in Figure 2, representing the secondary creep stage, is described by:

$$\varepsilon_c = \eta_1 + \eta_2 \zeta \tag{10}$$

Second, the parameter η_4 is fitted according to the shape of the creep curve covering both the primary and secondary stages. The blue line in Figure 2, corresponding to the first two stages, is expressed as:

$$\varepsilon_c = \eta_1 (1 - e^{-\eta_4 \zeta}) + \eta_2 \zeta \tag{11}$$

Finally, parameters η_5 and η_6 are determined by matching the shape of the tertiary creep stage. These are further optimized by fitting the full three-stage creep curve. The red line in Figure 2, representing the complete creep behavior, is modeled by Equation (2).

Table 2 - Dimensionless coefficients (a_i, b_i, c_i, d_i) of dimensionless creep model parameters of DZ411 superalloy for 6-parameter methods.

η_i	a_i	b_i	c_i	d_i
η_1	-1.9736	-1.5095	1.5955	1.2203
η_2	0.4596	0.3515	0.4103	0.3138
η_3	5.8644	-7.7892	2.9061	-0.0313
η_4	4.4176	3.3787	-1.3353	-1.0213
η_5	1.2141	0.9286	-1.0304	-0.7881
η_6	0.0225	0.0172	0.0440	0.0336

Based on creep test data of DZ411 superalloy under various conditions, the creep strain-time curves were fitted using the physically well-defined Equation (2) to determine the corresponding coefficients η_i. Equation (2) accurately captures all three stages of the creep curve. The data were further fitted using Equation (5), and the resulting coefficients of the dimensionless creep model parameters are provided in Table 2. The parameter set was used to predict the normalized time creep curves.

Further analysis of the parameters η_1, η_2, and η_3 in Equation (2) demonstrates that in the creep deformation tests of the DZ411 superalloy, the decelerating (primary) creep stage accounts for the smallest proportion of the total creep strain, whereas the accelerating (tertiary) creep stage delivers the most significant contribution. Additionally, the fitted parameters η_4, η_5, and η_6 reveal that the transition rate from the primary to the steady-state stage outpaces that from the steady-state to the tertiary stage. All material parameters required to execute the finite element calculations can be seamlessly integrated into the user subroutine, which has been successfully compiled within the finite element software environment.

3. High Temperature Creep Test

3.1 Material

The material used in this study is DZ411, a nickel-based, precipitation-strengthened, directionally solidified (DS) superalloy designed for service at temperatures below 1000 °C. It was fabricated by vacuum induction melting followed by directional solidification at a mold temperature of 1520 ± 20 °C and a withdrawal rate of 5 ± 1 mm/min. The alloy's chemical composition (in weight percent) is:

Table 3 - Chemical composition of DZ411 superalloy (wt.%).

C	Cr	Ni	Co	W	Mo	Al	Ti	Ta
0.07~0.12	13.5~14.3	Bal.	9.0~10.0	3.5~4.1	1.3~1.7	2.8~3.4	4.6~5.2	2.5~3.1
B	S	P	Si	Pb	Bi	As	Sn	Sb
0.007~0.02	≤0.01	≤0.005	≤0.2	≤0.0005	≤0.0001	≤0.005	≤0.002	≤0.001

Note: All values are given in mass fraction (wt.%). "Bal." indicates nickel as the balance element.

Figure 3 illustrates the typical scanning electron microscopy (SEM) micrograph of the initial microstructure of the studied DZ411 superalloy prior to high-temperature creep testing. The material exhibits a classical coherent two-phase configuration, where highly ordered, cuboidal γ' strengthening precipitates are uniformly embedded within the continuous, orthogonal γ matrix channels. The γ' phases feature a highly regular arrangement with sharp interfaces and a distinct cubic morphology, while the narrow γ channels provide primary pathways for early-stage dislocation motion and slip line formation. This pristine, well-defined cuboidal morphology serves as the structural baseline for analyzing subsequent microstructural degradation, such as the directional coarsening and rafting behavior of γ' phases, under long-term thermal-mechanical coupling environments.

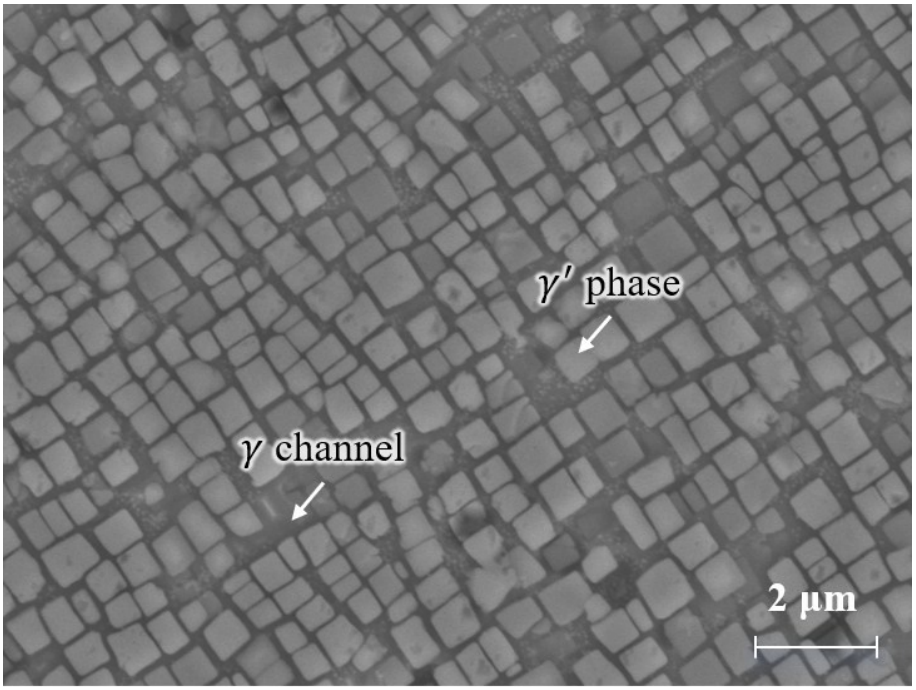


Figure 3 – Typical SEM micrograph showing the initial microstructure of the DZ411 superalloy, consisting of cuboidal γ' phases and continuous γ matrix channels.

3.2 Specimen Geometry and Testing System

To evaluate the creep mechanical behavior of the material under complex multiaxial stress states, a cylindrical circumferentially notched round bar specimen was employed in this study. The detailed geometric dimensions of the specimen are schematically illustrated in Figure 4. The total length of the specimen is 82 mm, with M14×1.0 threads machined at both ends to connect with the testing machine grips, thereby ensuring strict coaxiality during the loading process. The length of the parallel section is 35 mm, featuring a gross diameter (nominal outer diameter) of $D = 6$ mm. A circumferential notch is machined precisely at the center of the specimen, where the net-section diameter at the notch root is $d = 4.4$ mm and the notch root radius is $r = 0.8$ mm. A transition radius of 15 mm (R15) is implemented to mitigate stress concentration between the gripping ends and the gauge section. This specific notch configuration is designed to introduce a target stress triaxiality at both the notch root and the specimen core, effectively replicating and testing the localized constraint effects and creep damage rupture mechanisms of engine high-temperature pressure-retaining components under actual service environments.

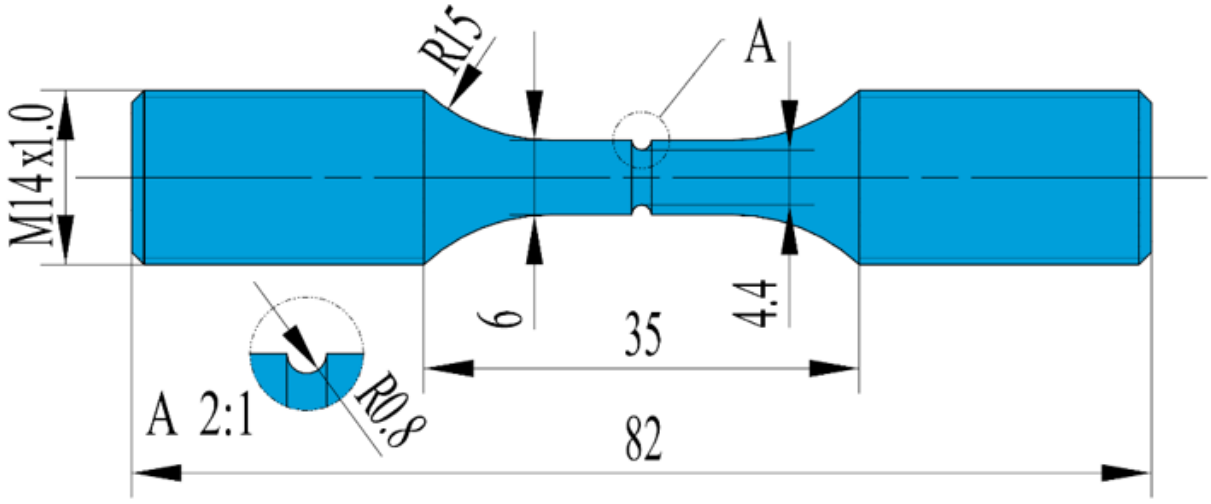


Figure 4 – Geometry and dimensions of the circumferentially notched specimen (unit: mm).

The high-temperature creep tests in this study were performed on a QBR-100 creep-rupture testing machine, which features a maximum axial load capacity of 100 kN. To guarantee precise coaxiality under high-temperature and long-term loading conditions, and to minimize the impact of additional bending moments on the multiaxial stress field at the notch, a high-precision threaded sleeve gripping method was adopted. By precisely screwing the M14×1.0 male threads at both ends of the specimen into the internally threaded high-temperature pull-rods made of a nickel-based superalloy (e.g., GH4169), a rigid and well-aligned connection with the loading system was achieved.

Table 4 - High-temperature creep test matrix and loading conditions for DZ411 superalloy specimens.

Test specimen	Temperature / ℃	Stress / MPa	Rupture life / h
SC-1	850	540	393.80
SC-2	850	510	513.83
SC-3	930	340	215.33
SC-4			242.54
SC-5	930	320	283.00
SC-6			242.57



Figure 5 – High-temperature creep and rupture testing machines.

The mechanical loading and temperature control matrices are summarized in Table 4, comprising two temperature series at 850°C and 930°C executed under a constant axial tensile load control mode. Since the circumferentially notched specimen possesses a minimum net-section diameter of 4.4 mm at the notch root, corresponding to a net cross-sectional area (A_{net}) of approximately 15.21 mm², the target axial tensile force was applied based on the nominal net-section stress of each specimen. Specifically, under the 850°C condition, specimens SC-1 and SC-2 were tested at constant nominal net-section stresses of 540 MPa and 510 MPa, respectively, requiring a maximum target axial load of approximately 8.21 kN; under the 930°C condition, the test stresses for specimens SC-3 and SC-5 were set to 340 MPa and 320 MPa, respectively, with SC-4 and SC-6 reserved for subsequent parameter adjustments. During testing, the specimens were heated using a high-

precision three-zone split electrical resistance furnace, and three routes of K-type thermocouples were symmetrically attached adjacent to the notch to monitor real-time temperature fluctuations within the gauge section. Throughout the creep exposure, an intelligent control system strictly maintained both the spatial temperature gradient and temporal fluctuations within ±1°C. Upon reaching the target temperature, a 1 h thermal soaking period was enforced to ensure complete thermal equilibrium between the specimen core and the gripping assemblies, followed by a smooth, shock-free application of the target load, with creep deformation data continuously recorded until specimen rupture.

3.3 Testing Results

The experimental rupture lives of the DZ411 superalloy specimens with circumferential notches, tested under varying thermomechanical conditions, are summarized in Table 4. Experimental results demonstrate that the rupture life is highly sensitive to both the applied stress and test temperature. At a constant temperature of 850 °C, reducing the applied stress from 540 MPa to 510 MPa resulted in a noticeable extension of the rupture life from 393.80 h to 513.83 h. When the test temperature was elevated to 930 °C, the specimens exhibited a more pronounced susceptibility to stress variation. Specifically, within the stress range of 320 MPa to 340 MPa, the measured rupture lives were 215.33 h, 242.54 h, 283.00 h, and 242.57 h, respectively. The observed variations in rupture life among specimens tested under identical nominal conditions (e.g., SC-4 and SC-6) are primarily attributed to the localized microstructural heterogeneity and the inherent scatter associated with notch-sensitivity in high-temperature creep experiments. These quantitative data provide a robust basis for validating the proposed creep-rupture life prediction model and highlight the complex interaction between geometric constraint and material degradation at elevated temperatures.

4. Finite Element Analysis

4.1 Finite Element Modeling and Preprocessing

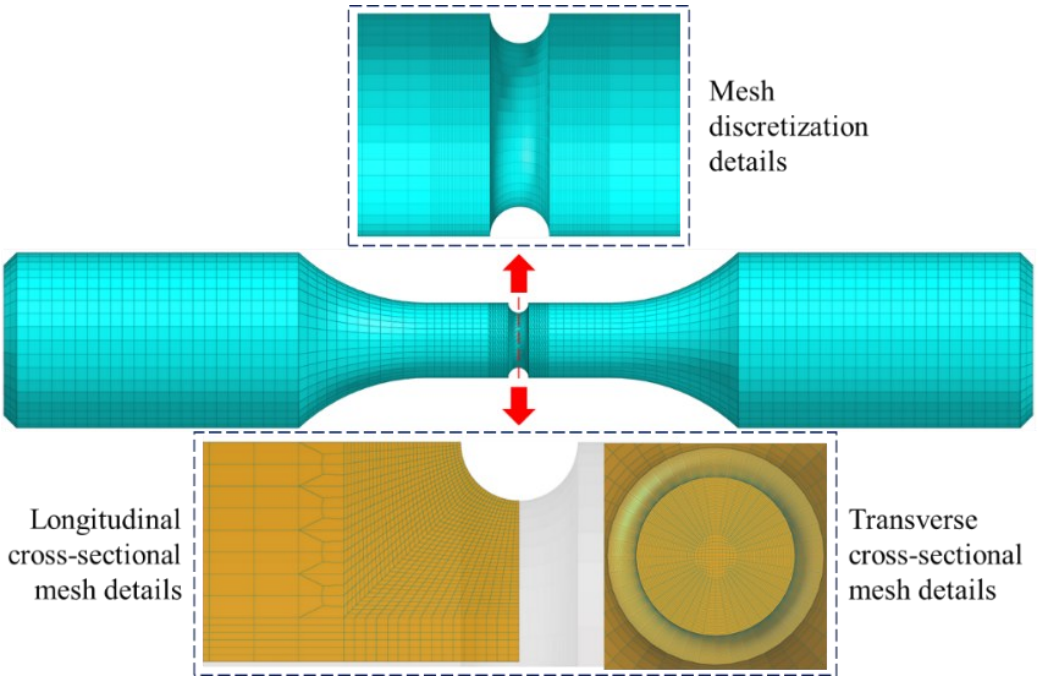


Figure 6 – Finite element meshing of the geometric model.

The developed creep constitutive model was implemented into a commercial finite element software, enabling finite element simulations based on the three-stage creep model. In this study, a full three-dimensional finite element model of the circumferentially notched specimen was constructed, utilizing high-quality structured hexahedral elements for complete spatial discretization. Given the severe stress concentration inherent to the notch root, a localized gradient mesh refinement strategy was implemented. The mesh density was strategically intensified within the immediate vicinity of the

notch root to precisely capture the high-gradient stress and strain fields, thereby effectively circumventing numerical singularities and mitigating mesh sensitivity. Conversely, the elements smoothly transition to a coarser configuration in regions remote from the notch to optimize computational efficiency. Based on a comprehensive mesh independence verification, the calculated stress distributions under the current mesh density have achieved complete convergence.

Appropriate boundary conditions and loading were applied as Table 5, and finite element analyses were carried out.

Table 5 - Loading conditions for creep analysis cases of notched specimens.

Test specimen	Temperature / ℃	Stress / MPa	Calculation time / h
SC-1	850	540	400
SC-2	850	510	600
SC-3	930	340	250
SC-4, 5, 6	930	320	300

4.2 Contour Analysis of Multiaxial Stress and Damage Fields

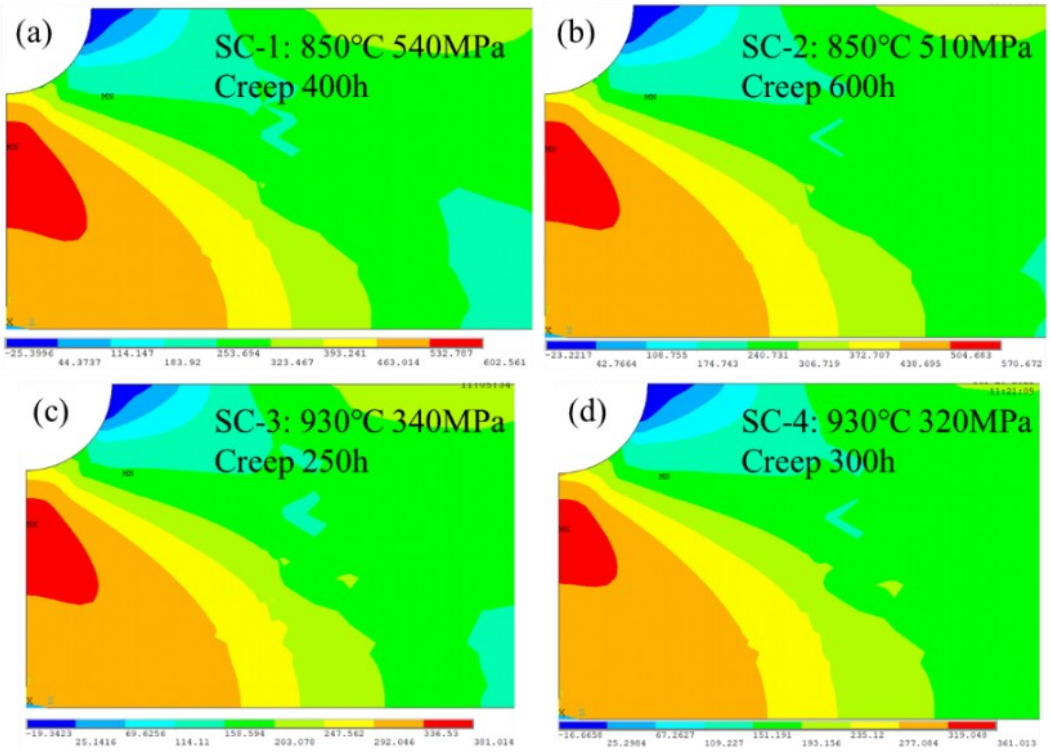


Figure 7 – Distribution of stress in the tensile direction after creep-induced stress relaxation.

Figure 7 presents the numerical contour plots of the first principal stress (σ_1) in the vicinity of the notch cross-section at the termination of computation under various loading conditions (SC-1 to SC-4). As illustrated, the stress field within the notch region exhibits highly pronounced characteristics of stress redistribution and stress relaxation throughout the high-temperature creep history. During the initial loading phase (i.e., the elasto-plastic loading stage), the maximum first principal stress typically concentrates in the immediate vicinity of the notch root surface due to the severe geometric discontinuity effect of the circumferential notch, manifesting a strong localized stress concentration. However, driven by the accumulation of creep time (e.g., 400 h for condition SC-1 and 600 h for condition SC-2), the material at the surface layer of the notch root experiences extremely high localized creep strain rates under the synergistic effects of elevated temperature and high stress, thereby inducing intense localized stress relaxation.

As depicted in the contours, the stress level significantly drops in the boundary region adjacent to

the circular notch surface, marked by the minimum point "MN" in blue and cyan zones. This visually demonstrates that the deformation resistance of the surface material undergoes an inward relaxation of elastic strain during long-term creep. As an inevitable consequence of this stress relaxation, the highly stressed zone (red region) of the entire stress field undergoes a distinct inward migration phenomenon. It can be clearly observed from Figure 7(a)–(d) that the maximum point of the first principal stress (denoted by the red "MX" point) has completely detached from the geometric boundary of the notch, significantly migrating radially toward the core of the specimen and establishing a stable high-stress peak plateau within the internal sub-surface layer.

The underlying physical mechanism governing this inward migration of the peak stress location originates from the unique multiaxial stress constraint effect of the notched specimen. Although the stress in the surface layer is relieved due to rapid creep deformation, the core material of the specimen remains under intense three-dimensional constraint from the surrounding geometric structure, thereby maintaining an exceptionally high stress triaxiality. Consequently, the externally applied axial load continuously shifts toward the under-relaxed core, leading to the inward migration of the stress peak. Under the 850 °C condition, the internal peak values of the maximum principal stress for conditions SC-1 and SC-2 are maintained at 602.6 MPa and 570.7 MPa, respectively; as the temperature elevates to 930 °C (SC-3 and SC-4), the relaxed internal stress peaks smoothly decline to 381.0 MPa and 361.0 MPa, respectively, due to the global thermal softening of the matrix material. This spatial reshaping behavior of the first principal stress from the surface to the interior directly dictates that subsequent microstructural creep voids and microcracks preferentially nucleate within the specimen core rather than on the surface, serving as a classic core mechanical mechanism governing notch damage evolution.

4.3 Stress Redistribution along Critical Paths

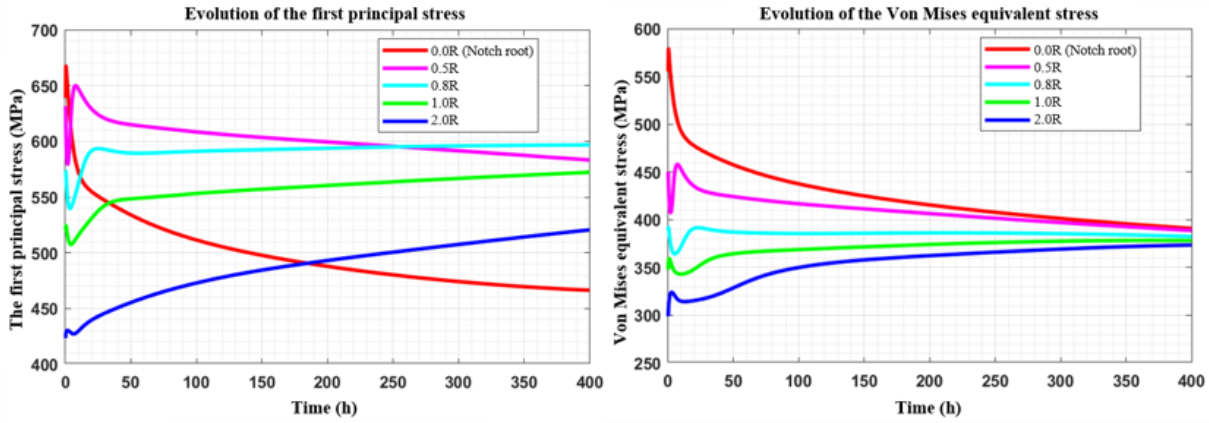


Figure 8 – Temporal evolution of (a) the first principal stress and (b) Von Mises equivalent stress at different positions.

To quantitatively analyze the stress fields ahead of the notch, Figure 8 displays the temporal evolution of the first principal stress (σ_1) and von Mises equivalent stress (σ_v) for the SC-1 specimen (850°C, 540 MPa), where 0.0R represents the notch root surface and 0.5R to 2.0R denote increasing depths toward the core. As shown in Figure 8(a), σ_1 exhibits clear load shedding from the surface to the interior during creep, where at the notch root (0.0R), σ_1 initially peaks at 670 MPa due to geometric stress concentration, then rapidly relaxes within the first 50 h, decaying to 465 MPa at 400 h, representing a 30.6% reduction. Within the interior (0.5R to 2.0R), as surface stress relaxes, the applied load shifts to the under-deformed core, causing σ_1 to rise at inner depths; notably, at 2.0R, it increases monotonically from 425 MPa to 520 MPa, confirming the inward migration of the peak principal stress. Figure 8(b) illustrates that while the von Mises stress (σ_v) at the notch root (0.0R) relaxes from 580 MPa to 390 MPa, it converges tightly into a narrow band of 370-390 MPa across all internal depths (0.5R to 2.0R) after entering the steady-state creep regime beyond 100 h. These results indicate that while the von Mises stress homogenizes across the net section due to visco-plastic flow, the first principal stress (σ_1) continually shifts inward under multiaxial constraints, providing the fundamental mechanical explanation for why long-term creep damage preferentially initiates in the sub-surface of notched specimens.

5. Rupture Life Prediction Based on the Stress Relaxation Effect

5.1 Evolution of Stress Triaxiality

To further quantitatively evaluate the degree of localized multiaxial stress constraint induced by the notch and its potential impact on creep damage evolution, stress triaxiality (*TF*) is introduced as a core mechanical parameter. Stress triaxiality is defined as the ratio of hydrostatic stress to von Mises equivalent stress, expressed mathematically as:

$$TF = \frac{\sigma_{\mathrm{m}}}{\sigma_{\mathrm{V}}} \tag{12}$$

where σ_{V} is the von Mises equivalent stress and σ_m is the hydrostatic stress calculated from the three principal stresses:

$$\sigma_{\mathrm{m}} = \frac{1}{3}\left(\sigma_1 + \sigma_2 + \sigma_3\right) \tag{13}$$

Under multiaxial stress conditions, the stress triaxiality factor is introduced to identify the critical location and timing of damage initiation [7]. Finite element simulations show that as creep progresses, the stress distribution gradually becomes stable and more uniform, and the stress triaxiality factor also stabilizes. The spatial location dynamic corresponding to the maximum stress triaxiality along the bisector line of the notch root is defined as the critical point. The peak stress at this location after stress redistribution has stabilized is taken as the input parameter for the rupture life equation. Rupture life predictions are then performed based on this reference stress.

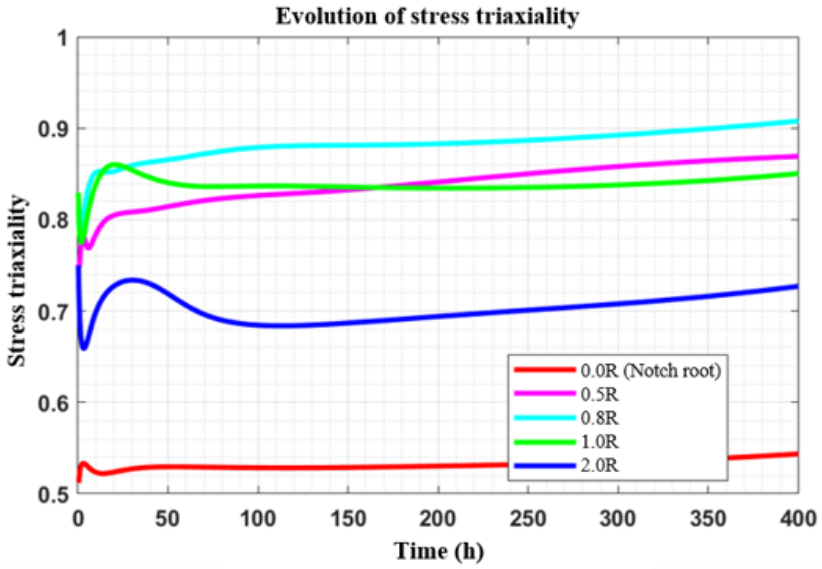


Figure 9 – Temporal evolution of the stress triaxiality factor at various normalized radial positions across the notch section for specimen SC-1 (R: notch root radius).

The magnitude of *TF* directly indicates the degree of hydrostatic constraint exerted on a local material element by the surrounding structure, where elevated stress triaxiality generally suppresses plastic flow, accelerates micro-void nucleation and growth, and significantly reduces creep ductility. Figure 9 displays the temporal evolution of *TF* at various radial depths for the SC-1 specimen during the 400 h creep history, revealing highly distinct and spatially dependent evolutionary profiles driven by high-temperature stress redistribution. At the notch root surface (0.0R), the absence of radial constraint near the free boundary keeps *TF* at the lowest level throughout the exposure, hovering stably within a low plateau of 0.52-0.54, which indicates that a low multiaxial constraint state dominates the surface layer to favor deformation relaxation over damage accumulation.

Conversely, the sub-surface regions close to the core (0.5R and 0.8R) exhibit the most pronounced upward climb, particularly at 0.8R where *TF* increases monotonically from an initial value of 0.80 to approximately 0.91 at 400 h due to localized creep flow and inward load shedding, making it the most severely constrained region across the net section, while the 0.5R location exhibits a similar

rising trend to reach approximately 0.87. Within the specimen interior and along the central axis (1.0R and 2.0R), the 1.0R location undergoes a rapid transient peak of about 0.86 within the first 20 h due to initial plastic relaxation before slightly decreasing and stabilizing around 0.84 during the long-term steady-state stage, whereas the central axis (2.0R), after a brief drop during initial loading caused by complex stress wave interaction effects, enters a slow upward trajectory after 100 h and eventually stabilizes at around 0.73. Comprehensive comparison between the first principal stress and von Mises stress evolution reveals that while the von Mises stress across all internal depths (0.5R to 2.0R) tends to converge uniformly due to visco-plastic flow during long-term creep, the hydrostatic stress σ_m sustained by the elevated first principal stress remains high due to intense geometric constraints at the core. This directly causes *TF* within the sub-surface region (especially the 0.5R-1.0R interval) to stay persistently above a high value of 0.85. The superposition of this severe stress triaxiality and the inwardly migrated peak first principal stress establishes a highly destructive mechanical boundary condition, qualitatively and quantitatively explaining why creep cracks in this high-performance superalloy preferentially nucleate within the internal sub-surface and propagate outward.

5.2 Development of a Rupture Life Prediction Approach

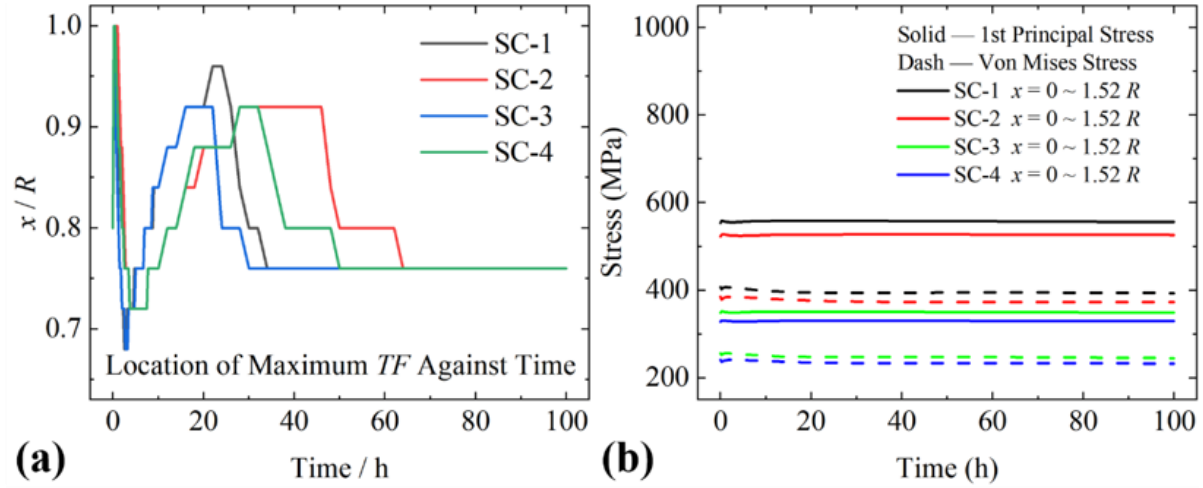


Figure 10 – Evolution of (a) maximum TF location and (b) process zone stresses against time.

Conventional notch rupture life prediction methods often yield conservative results by relying on the initial elasto-plastic stress state and ignoring creep-induced stress redistribution and load shedding. To address this, a novel prediction method is proposed based on the spatio-temporal evolution of the maximum triaxiality factor (TF) location, premised on the fact that localized creep damage is governed by a geometry-controlled steady-state process zone rather than a single-point stress. The method involves four sequential steps: (1) tracking the normalized radial coordinate (x/R) of the maximum triaxiality factor ($TF_{\max}$) over time via finite element simulations; (2) defining a characteristic distance Δd from the notch root to the stable $TF_{\max}$ location (x_{steady}/R) reached during steady-state creep, establishing an annular process zone within $2 \times \Delta d$ to encompass intense multiaxial constraints; (3) calculating a representative reference stress (σ_{ref}) by averaging the Von Mises stress (σ_{v}) within this process zone ($x = 0 - 1.52R$ in this study); and (4) substituting σ_{ref} into the Larson-Miller (L-M) equation to predict long-term rupture life.

Figure 10 illustrates the temporal evolution of characteristic parameters under loading conditions of SC-1 to SC-4, validating the proposed model. As shown in Figure 10(a), the spatial location of $TF_{\max}$ exhibits a two-stage evolution: an initial transient phase (0-40 h) characterized by rapid inward migration and temperature-dependent oscillations due to differing thermal softening rates, followed by a steady-state convergence phase (>60 h) where all curves perfectly converge to a horizontal line at $x/R \approx 0.76$. This high consistency demonstrates that the process zone boundary is inherently dictated by the notch geometry, justifying the averaging zone of $x = 0 - 1.52R$ used in Figure 10(b). Furthermore, Figure 10(b) shows that the process-zone-averaged von Mises stress remains

remarkably constant during steady-state creep (beyond 40 h) with negligible time dependence. This constancy satisfies the strict requirement of a time-independent reference stress for the L-M equation, fundamentally ensuring the stability and reliability of the proposed life prediction model.

5.3 Rupture Life Prediction Results

To comprehensively validate the proposed modified reference stress life prediction model, Figure 11 quantitatively compares the predicted rupture lives, obtained by substituting the reference stress from the steady-state process zone ($x = 0 - 1.52R$) into the Larson-Miller (L-M) equation, with the experimental rupture lives. In this figure, the solid line represents the perfect prediction line ($t_{\text{pred}} = t_{\text{exp}}$), while the dashed lines define the conventional factor-of-two scatter band ($\pm 2 \times$ error band) commonly used in engineering creep analysis.

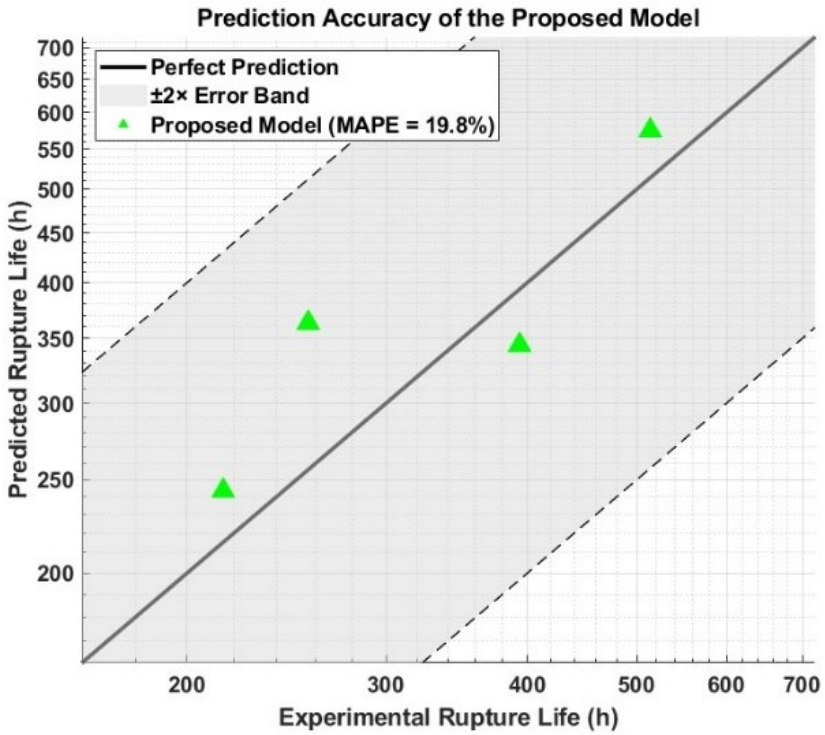


Figure 11 – Experimental results of creep rupture life for circumferentially notched DZ411 superalloy specimens under varying test conditions.

The comparison demonstrates that the model yields exceptionally high accuracy, with all predicted data points across various temperatures (850°C and 930°C) and stress levels tightly clustering along the perfect prediction line and falling 100% within the $\pm 2 \times$ error band. Such performance is highly outstanding given the complex micro-mechanisms and inherent scatter of notch creep rupture data. Quantitatively, the mean absolute percentage error (MAPE) is only 19.8%, which provides a high level of quantitative fidelity that fully satisfies the stringent design and safety assessment requirements for high-temperature engine components. The superior accuracy of this model fundamentally stems from its departure from conventional approaches relying on single-point initial or transient elastic stress states; instead, by tracking the spatio-temporal evolution of $TF_{\max}$, the proposed method successfully captures the spatial reshaping history of the stress field driven by stress relaxation and inward load shedding ahead of the notch front. Spatial averaging within the geometry-dominated steady-state process zone yields a reference stress that realistically reflects the global creep damage driving force within the highly constrained multiaxial region. Consequently, this model not only eliminates numerical singularities from initial transient calculations but also accurately accounts for the influences of temperature and loading variations on visco-plastic rheological behavior. Ultimately, this modeling strategy, which bridges microstructural damage mechanisms and macroscopic structural geometric constraints, provides a highly accurate and robust pathway for the long-term rupture life prediction of circumferentially notched components.

6. Conclusion

This study examined the creep deformation and rupture life of circumferentially notched DZ411 nickel-based superalloy specimens under elevated temperatures and various loads. Finite element simulations using a three-stage creep constitutive model were validated against high-temperature creep tests. The main findings are:

(1) The three-stage creep model, which captures all three creep stages, was successfully implemented into a commercial finite element code via a user subroutine, enabling accurate simulation of stress relaxation and redistribution in notched geometries.

(2) Creep-induced stress relaxation at the notch root significantly altered the local stress state, producing a strengthening effect that was systematically analyzed.

(3) With increasing creep time, stress relaxation led to continuous evolution of stress triaxiality at the notch, which was quantified throughout the redistribution process.

(4) A rupture life prediction method accounting for stress concentration effects was developed; predictions agreed well with experiments, all falling within a ±2 scatter band.

7. Contact Author Email Address

Mail to Shun Yang: yangshun_academic@buaa.edu.cn

8. Copyright Statement

The authors confirm that they, and/or their company or organization, hold copyright on all of the original material included in this paper. The authors also confirm that they have obtained permission, from the copyright holder of any third party material included in this paper, to publish it as part of their paper. The authors confirm that they give permission, or have obtained permission from the copyright holder of this paper, for the publication and distribution of this paper as part of the ICAS proceedings or as individual off-prints from the proceedings.

Acknowledgement

This work is supported by the National Science and Technology Major Project (No.J2019-IV-0012-0080), the National Natural Science Foundation of China (Nos.12472208, 12202030), the foundation of the State Key Laboratory of Structural Analysis, Optimization and CAE Software for Industrial Equipment (No.GZ24122), the foundation of the Opening Project of State Key Laboratory of Advanced Ceramics (No.SKL202408SIC), the foundation of the State Key Laboratory for Strength and Vibration of Mechanical Structures (No.SV2024-KF-14) and the Young Elite Scientists Sponsorship Program of the Beijing High Innovation Plan (No.20251051). We are grateful to the Analysis & Testing Center of Beihang University for the facilities, and the scientific and technical assistance.

References

[1] Ren, X., Li, F., Wen, Z. X., Cheng, H., and Yue, Z. F. *Calibrated the direct current potential drop method for fatigue crack propagation testing of nickel-based superalloy with film cooling hole* [J]. Theoretical and Applied Fracture Mechanics, 2024.

[2] Blachnio, J., Spychala, J., and Zasada, D. *Analysis of structural changes in a gas turbine blade as a result of high temperature and stress* [J]. Engineering Failure Analysis, 2021.

[3] Huang, J., Shi, D. Q., Yang, X. G., and Hu, X. A. *Effect of multi-axial stress state on creep behavior and stress rupture life of a Ni-based DS superalloy* [J]. Computational Materials Science, 2014.

[4] Liu, D. S., Zhang, D. X., Liang, J. W., Wen, Z. X., and Yue, Z. F. *Prediction of creep rupture life of a V-notched bar in DD6 Ni-based single crystal superalloy* [J]. Materials Science and Engineering a-Structural Materials Properties Microstructure and Processing, 2014.

[5] Shi, D., Li, Z., Yang, X., and Wang, H. *Accelerated LCF-creep experimental methodology for durability life evaluation of turbine blade* [J]. Fatigue & Fracture of Engineering Materials & Structures, 2018.

[6] Shi, D. Q., Quan, C. B., Niu, H. W., and Yang, X. G. *Constitutive modelling and creep life prediction of a directionally solidified turbine blade under service loadings* [J]. Materials at High Temperatures, 2015.

[7] Peng, J., Wang, Y., Dai, Q., Liu, X. D., Liu, L., and Zhang, Z. H. *Effect of Stress Triaxiality on Plastic Damage Evolution and Failure Mode for 316L Notched Specimen* [J]. Metals, 2019.